Applied Catalysis B: Environmental 243 (2019) 490–501

Contents lists available at ScienceDirect

Applied Catalysis B: Environmental

journal homepage: www.elsevier.com/locate/apcatb

Effect of support oxygen storage capacity on the catalytic performance of Rh nanoparticles for CO_2 reforming of methane

Ioannis V. Yentekakis[a,*,1], Grammatiki Goula[a,1], Maria Hatzisymeon[a,1], Ioanna Betsi-Argyropoulou[a,1], Georgia Botzolaki[a,1], Kalliopi Kousi[b], Dimitris I. Kondarides[b], Martin J. Taylor[c], Christopher M.A. Parlett[d,e], Amin Osatiashtiani[c], Georgios Kyriakou[c,*], Juan Pedro Holgado[f], Richard M. Lambert[f,g]

[a] Laboratory of Physical Chemistry & Chemical Processes, School of Environmental Engineering, Technical University of Crete, GR-73100, Chania, Crete, Greece
[b] Department of Chemical Engineering, University of Patras, GR-26500, Patras, Greece
[c] European Bioenergy Research Institute and Chemical Engineering & Applied Chemistry, Aston University, Aston Triangle, Birmingham, B4 7ET, United Kingdom
[d] The School of Chemical Engineering and Analytical Science, The University of Manchester, Manchester, M13 9PL, United Kingdom
[e] The University of Manchester at Harwell, Diamond Light Source, Harwell Campus, Didcot, OX11 0DE, United Kingdom
[f] Instituto de Ciencia de Materiales de Sevilla (CSIC), Americo Vespucio 49, 41092, Seville, Spain
[g] Department of Chemistry, Cambridge University, Cambridge, CB2 1EW, United Kingdom

ARTICLE INFO

Keywords:
Dry reforming of methane
Active sites
Synthesis gas
Rhodium nanoparticles
Support effects
CO_2 activation
Oxygen storage capacity
Resistance to carbon deposition
Oxygen ions spillover

ABSTRACT

The effects of the metal oxide support on the activity, selectivity, resistance to carbon deposition and high temperature oxidative aging on the Rh-catalyzed dry reforming of methane (DRM) were investigated. Three Rh catalysts supported on oxides characterized by very different oxygen storage capacities and labilities (γ-Al_2O_3, alumina-ceria-zirconia (ACZ) and ceria-zirconia (CZ)) were studied in the temperature interval 400–750 °C under both integral and differential reaction conditions. ACZ and CZ promoted CO_2 conversion, yielding CO-enriched synthesis gas. Detailed characterization of these materials, including state of the art XPS measurements obtained via sample transfer between reaction cell and spectrometer chamber, provided clear insight into the factors that determine catalytic performance. The principal Rh species detected by post reaction XPS was Rh^0, its relative content decreasing in the order Rh/CZ(100%) > Rh/ACZ(72%) > Rh/γ-Al_2O_3(55%). The catalytic activity followed the same order, demonstrating unambiguously that Rh^0 is indeed the key active site. Moreover, the presence of CZ in the support served to maintain Rh in the metallic state and minimize carbon deposition under reaction conditions. Carbon deposition, low in all cases, increased in the order Rh/CZ < Rh/ACZ < Rh/γ-Al_2O_3 consistent with a bi-functional reaction mechanism whereby backspillover of labile lattice O^{2-} contributes to carbon oxidation, stabilization of Rh^0 and modification of its surface chemistry; the resulting O vacancies in the support providing centers for dissociative adsorption of CO_2. The lower apparent activation energy observed with CZ-containing samples suggests that CZ is a promising support component for use in low temperature DRM.

1. Introduction

Synthesis gas (H_2+CO) is a critical intermediate in the chemical industry used as a feedstock for the production of hydrogen, ammonia, and Fischer-Tropsch-derived liquid energy carriers [1–6]. Accordingly, its production by means of hydrocarbon reforming has attracted much academic and industrial interest. Currently, due to the abundance of natural gas, methane is most commonly employed for this purpose, while locally produced biogas is emerging as an attractive alternative feedstock [7,8]. Methane reforming can be achieved by reaction with steam, CO_2 (dry reforming, DRM, reaction 1) or by partial oxidation with O_2.

$$CH_4 + CO_2 \leftrightharpoons 2CO + 2H_2 \quad \Delta H^{o}_{298} = 247\ kJ\ mol^{-1} \qquad (1)$$

The recent resurgent interest in DRM in part reflects the fact that both reactants are important greenhouse gases. Moreover, compared to

* Corresponding authors.
E-mail addresses: yyentek@isc.tuc.gr (I.V. Yentekakis), g.kyriakou@aston.ac.uk (G. Kyriakou).
[1] www.pccplab.tuc.gr.

https://doi.org/10.1016/j.apcatb.2018.10.048
Received 26 July 2018; Received in revised form 10 October 2018; Accepted 22 October 2018
Available online 28 October 2018
0926-3373/

steam reforming or partial oxidation, DRM offers the advantage of producing synthesis gas with a molar H_2/CO ratio close to unity, which is ideal for the Fischer–Tropsch industry [1–6,9–14]. In addition, the reaction provides a route for direct utilization of biogas produced via anaerobic microbial digestion or fermentation of biomass (waste water treatment facilities, agriculture wastes) which consists mainly of CH_4 (50–70%) and CO_2 (25–50%) [7,8]. Furthermore, internal reforming of biogas by means of DRM enables its use in directly-fuelled solid oxide fuel cells, which are efficient and eco-friendly devices for the generation of electrical power [7,15–18].

Due to its high endothermicity, DRM is typically operated in the temperature range 650–800 °C, conditions under which a number of side reactions are also favored, including the reverse water gas shift reaction (reaction 2), methane cracking (reaction 3), the Boudouard reaction (reaction 4) and carbon oxidation reactions (reactions 5–7) [19–21]:

$$H_2 + CO_2 \leftrightharpoons CO + H_2O \qquad \Delta H^o_{298} = +41\ kJ\ mol^{-1} \quad (2)$$

$$CH_4 \leftrightharpoons 2H_2 + C \qquad \Delta H^o_{298} = +75\ kJ\ mol^{-1} \quad (3)$$

$$2CO \leftrightharpoons CO_2 + C \qquad \Delta H^o_{298} = -172\ kJ\ mol^{-1} \quad (4)$$

$$C + O_2 \rightarrow CO_2 \qquad \Delta H^o_{298} = -394\ kJ\ mol^{-1} \quad (5)$$

$$C + \tfrac{1}{2}\ O_2 \rightarrow CO \qquad \Delta H^o_{298} = -110\ kJ\ mol^{-1} \quad (6)$$

$$C + H_2O \rightarrow CO + H_2 \qquad \Delta H^o_{298} = +131\ kJ\ mol^{-1} \quad (7)$$

Reactions (2)–(7) affect both the H_2/CO ratio and as a result of cumulative carbon deposition, the catalyst's lifetime which is a major problem in many catalytic systems that have been investigated for DRM [1–6]. Consequently, development of selective and robust DRM catalysts, especially for use at intermediate temperatures, remains a major research challenge in the field of heterogeneous catalysis [6].

Due to their low cost, Ni-based catalysts have been extensively studied for DRM application, but they suffer from excessive carbon deposition and severe thermal sintering [2,3,10–13,20–27]. Partially successful attempts to reduce these adverse effects include the use of strongly basic supports and/or supports containing significant concentrations of oxygen ion vacancies, such as mixed metal oxides incorporating La_2O_3, CaO, Sm_2O_3, PrO_2, Yb_2O_3, ZrO_2 or CeO_2 [20–35]. For example, $Ce_xZr_{1-x}O_{2-\delta}$ composites, which are widely used in three-way catalytic chemistry due to their high oxygen storage capacity (OSC) [36–38], improved both the efficiency and long term stability of Ni catalysts in DRM [20,27,34,35]. Noble metal-based catalysts exhibit comparable DRM activity to Ni formulations, but also greater resistance to carbon deposition, [3,9–11,39–47], which offsets their high cost for potential large-scale application.

Because of their favorable resistance to both sintering and coking [44–49], Rh catalysts have recently attracted much interest due to their promising performance in methane reforming by means of steam-, oxy-, di- and tri-reforming methodologies [26,50–54]. To our knowledge, the only work related to the use of $Ce_xZr_{1-x}O_{2-\delta}$-based supports for Rh-based catalysts is that of Yuan et al. [55], who investigated the effect of ceria-zirconia doping on the performance of Rh/MgO catalysts in the auto-thermal steam reforming of methane ($CH_4 + H_2O + O_2$). They found that $Ce_{0.5}Zr_{0.5}O_{2-\delta}$/MgO induced significant enhancement of both catalyst stability and selectivity towards H_2 formation, the latter ascribed to increased water gas shift activity. In comparison, Rh-catalyzed DRM has received less attention and there are no reports on the effect of incorporating CeO_2-ZrO_2 containing composites into such catalysts.

Here we report the DRM catalytic behavior of well-characterized Rh nanoparticles supported on three different oxides with very different lattice oxygen labilities ranging from γ-Al_2O_3, to alumina-ceria-zirconia (ACZ: 80 wt% Al_2O_3-20 wt% $Ce_{0.5}Zr_{0.5}O_{2-\delta}$) to ceria-zirconia (CZ: $Ce_{0.5}Zr_{0.5}O_{2-\delta}$). The oxygen ion lability (or lack of it) characteristic of these materials is related to their O^{2-} mobility and oxygen storage capacity, which determine their propensity to provide spillover oxygen to metal particles dispersed on their surfaces [56–60]. This property can strongly modify the intrinsic catalytic activity of metal nanoparticles [56–60] and the investigation of such effects in the context of Rh-catalyzed DRM is the main objective of the present investigation. Catalytic measurements were carried out over a wide range of conditions over well-characterized samples and supplemented by state of the art XPS measurements involving in situ sample transfer between reaction cell and spectrometer chamber, without exposure to laboratory air. It was unambiguously demonstrated that Rh^0 species are the principal active sites for methane activation, stabilized by O^{2-} backspillover from the two CeO_2-containing metal oxides that possess high oxygen ion lability. The corresponding catalysts exhibited enhanced selectivity towards CO-enriched syngas formation, ascribed to the ease of formation of O^{2-} vacancies that acted as centers for dissociative adsorption of CO_2. They were also characterized by lower apparent activation energies, which is of particular interest with respect to low-temperature DRM applications. The results are rationalized in terms of a detailed bi-functional reaction mechanism involving both metal and oxide phases, including the effects of metal-support interaction.

2. Experimental

2.1. Catalyst preparation

Rhodium (III) nitrate solution (10%w/v Rh in 20–25 wt% HNO_3) was purchased from Acros Organics. $Al(NO_3)_3{\cdot}9H_2O$, $Zr(NO_3)_2{\cdot}H_2O$ and $Ce(NO_3)_3{\cdot}6H_2O$ were supplied by Alfa Aesar and γ-Al_2O_3 powder was obtained from Engelhard. Alumina-ceria-zirconia (ACZ, 80 wt% Al_2O_3 - 20 wt% $Ce_{0.5}Zr_{0.5}O_{2-\delta}$) and ceria-zirconia (CZ, $Ce_{0.5}Zr_{0.5}O_{2-\delta}$) supports were prepared by co-precipitation of the corresponding metal precursor salts [61] followed by calcination at 800 °C for 1 h, whereas γ-Al_2O_3 was used as received.

Supported rhodium catalysts with a 1.0 wt% Rh nominal loading were prepared by the wet impregnation method. An appropriate amount of the support (γ-Al_2O_3, ACZ or CZ) was impregnated under continuous stirring at 75 °C in a 2 mg Rh/mL concentrated solution of $Rh(NO_3)_3$. After water evaporation, the sample was dried at 110 °C for 12 h and then calcined in air at 450 °C for 1 h for nitrate precursor decomposition. The resulting powder was reduced at 400 °C under 50% H_2/He flow for 2 h followed by heating (20 °C/min) under 1% H_2/He flow to 800 °C, maintained for 1 h. Catalysts thus prepared are denoted in the following as "fresh" samples (Table 1).

2.2. Characterization methods

Textural and structural characteristics (total surface areas, pore volumes, morphology, total metal contents and dispersion) and redox properties of the synthesized catalysts were determined by BET, High-Resolution Transmission Electron Microscopy (HRTEM), Powder X-Ray Diffraction (PXRD), Inductively Coupled Plasma - Optical Emission Spectroscopy (ICP-OES), Isothermal hydrogen chemisorption at 0 °C, and H_2-Temperature Programmed Reduction (H_2-TPR). Specifically:

2.2.1. BET measurements

Surface areas, average pore volume and mean pore size diameters were obtained from N_2 adsorption–desorption isotherms at −196 °C and relative pressures in the range 0.05–0.30 with a Quantachrome Nova 2200e.

2.2.2. TEM measurements

High-resolution TEM images were obtained with an aberration corrected JEOL 2100-F microscope operated at 180 kV. Samples were prepared by gently grinding the powders in methanol, subsequent deposition on 300-mesh carbon supported copper grids, then dried under ambient conditions. Image analysis was carried out using ImageJ 1.41 software.

Table 1
Textural and morphological characteristics of the supporting materials and the corresponding *fresh* Rh catalysts.

Supports and Catalysts	Chemical formula[a]	S_{BET} ($m^2\,g^{-1}$)	Total pore volume ($cm^3\,g^{-1}$)	Average pore size diameter (nm)	Rh Dispersion[b] (%)	Rh mean particle size (nm) measured by	
						H_2-chem	HRTEM
γ-Al_2O_3	γ-Al_2O_3	178	0.60	13.5		–	–
Rh/γ-Al_2O_3	1wt%Rh/γ-Al_2O_3	160	0.57	14.2	88.3	1.2	1.3 ± 0.4
ACZ	80 wt%Al_2O_3-20 wt%$Ce_{0.5}Zr_{0.5}O_{2-\delta}$	149	0.29	7.9		–	–
Rh/ACZ	0.8 wt%Rh/(80 wt%Al_2O_3-20 wt %$Ce_{0.5}Zr_{0.5}O_{2-\delta}$)	136	0.28	8.2	77.4	1.8	1.5 ± 0.5
CZ	$Ce_{0.5}Zr_{0.5}O_{2-\delta}$	22	0.05	9.2		–	–
Rh/CZ	0.8 wt%Rh/$Ce_{0.5}Zr_{0.5}O_{2-\delta}$	17	0.05	12.3	27.8	5.0	5.1 ± 1.7

[a] Rh content measured by means of ICP-OES.
[b] based on H_2 uptake values (42.9, 30.1 and 10.8 μmol $H_2\,g^{-1}$ for Rh/γ-Al_2O_3, Rh/ACZ and Rh/CZ respectively) measured by means of isothermal H_2 chemisorption at 0 °C.

2.2.3. PXRD measurements

Powder X-ray diffraction (PXRD) patterns were collected with a Bruker D8 Advance Diffractometer with a LynxEye high-speed strip detector using Cu $K_{\alpha 1}$ (λ = 0.1542 nm) radiation.

2.2.4. Inductively coupled plasma - optical emission spectroscopy (ICP-OES) measurements

Total Rh contents were obtained by means of ICP-OES using a Thermo Scientific iCAP 7400 duo instrument. Samples were digested in 5 mL HNO_3 (Fisher, 70%) and 100 mg NH_4F (Sigma Aldrich, ≥98.0%) at 190 °C via microwave irradiation (CEM–MARS microwave reactor). This was followed by addition of HCl (1 mL, Fisher, 37%) and the reactively formed HF, neutralized by addition of a boric acid solution (1 mL, Fisher, 3%). Subsequent analysis was carried out after sample dilution in 10% aqueous HNO_3.

2.2.5. Isothermal hydrogen chemisorption measurements

provided corroborating information about the number of Rh surface sites (i.e. Rh dispersion) and the associated crystallite sizes. Measurements were carried out on a Quantachrome ChemBet Pulsar TPR/TPD chemisorption analyzer equipped with an Omnistar/Pfeiffer Vacuum mass spectrometer. For this purpose, ~150 mg of catalyst was loaded into a quartz U-tube connected to the analyser and pre-treated as follows before H_2-Chemisorption measurements. The sample was reduced with a flux of 5% H_2 in He (15 N mL min^{-1}) at 550 °C for 1 h, followed by N_2 flux (15 N mL min^{-1}) at the same temperature for 0.5 h, then cooled to room temperature under N_2 flow. To avoid hydrogen spillover in the case of CeO_2-containing supports, samples were cooled to 0 °C in an ice/water bath. Pulses of pure hydrogen (280 μL) were injected until saturation, thus providing the total H_2 uptake of chemisorbed hydrogen. These values were used to estimate the number of active surface sites, and hence Rh dispersion, mean Rh crystallite size and Turnover Frequencies (TOFs).

2.2.6. Hydrogen temperature programmed reduction measurements

H_2-TPR measurements were carried out in the temperature interval 30–850 °C using the same instrumentation as employed for H_2-chemisorption experiments. To this end, ~150 mg of catalyst was loaded into a quartz U-tube connected to the TPR apparatus and pre-treated in situ with 20% O_2/He at 750 °C for 0.5 h (pre-oxidized), cooled to room temperature under the same atmosphere, then purged under He flow for 0.5 h. After this pre-treatment, a flow of 15 N mL min^{-1} of 1% v/v H_2 in He was continuously passed through the sample and a linear temperature ramp from ~30 °C up to 850 °C was applied at 10 °C min^{-1} and the H_2 content of the effluent gas (TPR spectra) was analyzed by MS.

2.2.7. Temperature programmed Oxidation (TPO) experiments on used samples

The amount and reactivity toward oxygen of carbonaceous species deposited on the used Rh catalysts were assessed by TPO. In a typical experiment, 100 mg of catalyst that had previously been exposed to reaction conditions for 3 h was placed in a quartz reactor, retained by means of quartz wool. A linear temperature ramp of 10 °C min^{-1} from room temperature to 750 °C was applied under a constant flow (30 $cm^3\,min^{-1}$) of 6.1% O_2 in He. Temperature was measured in the middle of the catalyst bed by means of a K-type thermocouple. Analysis of the exit gas was accomplished by on-line mass spectrometry (FL-9496 Balzers) continuously monitoring the signals at m/z = 32 (O_2), 28 (CO) and 44 (CO_2). Calibration of the mass spectrometer was performed by means of gas mixtures of known composition.

2.2.8. XPS measurements on fresh and used samples

X-ray photoelectron spectra were acquired using customized equipment incorporating a high temperature-high pressure cell (SPECS HPC-20) with infra-red sample heating. The cell design allowed sample heating up to 800 °C, under flow or static conditions, at pressures up to 20 bar. This arrangement enabled fast post-reaction sample transfer from the reaction chamber to the spectrometer chamber, whilst maintaining UHV conditions–i.e. without exposure to laboratory air. Spectra were obtained with a hemispherical analyzer (SPECS Phoibos 100) operated at fixed transmission and 50 eV pass energy with energy step 0.1 eV using a non-monochromatized X-ray source (Al Kα; 1486.6 eV). Binding energies were calibrated using Al 2p (74.0 eV) as an internal reference. This method of calibration was necessary because surface charging occurred under photoemission conditions. The effect was constant during data acquisition and never greater than 5 eV, thus causing no distortion of peak shapes. Prior to analysis, samples were evacuated to a base vacuum of 10^{-7} mbar at room temperature. In a typical experiment, the fresh, calcined catalyst sample was placed in the spectrometer chamber and the XP spectra were obtained. The sample was then transferred under vacuum to the high pressure cell were it was heated to 700 °C and exposed to a 50%:50% CH_4:CO_2 mixture for 3 h at a total pressure of 1 bar. After cooling to room temperature in reaction gas the samples were transferred back to the spectrometer chamber for analysis, without exposure to laboratory air.

2.2.9. Catalytic evaluation

Catalytic data were obtained using a 3 mm internal diameter tubular quartz, fixed bed, single-pass flow reactor, fed with an equimolar mixture of CO_2 and CH_4 ([CH_4] = 50%, [CO_2] = 50%) at 1 bar and loaded with 50 mg catalyst (grain size 180–250 μm) held between two quartz wool plugs; the catalyst temperature measured by a centered K-type thermocouple. Both integral (high conversions) and differential (low conversions) operation of the reactor were used to provide a more complete analysis of the catalytic behavior. The total biogas feed flow

rate was typically 100 N mL min^{-1} during acquisition of *light-off* data (integral operation), corresponding to a weight-basis gas hourly space velocity (WGHSV = F_t/w_{cat}) value of 120,000 N mL g^{-1} h^{-1}. Turnover frequency (TOF) data were acquired at low CH_4 and CO_2 conversion (ca. 5–15 %; differential operation) by adjusting the total feed flow rate between 100–300 NmL min^{-1}. The durability of the catalysts under thermal sintering in an oxidative environment was examined by in situ sintering at 750 °C for 2 h under 20% O_2/He flow. The experimental set up is shown schematically in Fig. S1 (supplementary material).

The following equations were used to calculate CH_4 and CO_2 conversions (X_{CH4} and X_{CO2}), H_2 and CO yields (Y_{H_2} and Y_{CO}) and H_2/CO molar ratio:

$$X_i(\%) = 100(F_{t,in}[i]_{in}-F_{t,out}[i]_{out})/F_{t,in}[i]_{in} \qquad i = CH_4 \text{ or } CO_2 \quad (8)$$

$$Y_{H_2}\ (\%) = 100F_{t,out}\ [H_2]_{out}/2F_{t,in}[CH_4]_{in} \quad (9)$$

$$Y_{CO}(\%) = 100F_{t,out}[CO]_{out}/(F_{t,in}[CH_4]_{in}+F_{t,in}[CO_2]_{in}) \quad (10)$$

$$H_2/CO = [H_2]_{out}/[CO]_{out} \quad (11)$$

where $F_{t,in}$ and $F_{t,out}$ is the total flow rate at the reactor inlet and outlet, respectively, and the symbols in brackets are the concentrations of the corresponding reactants and products.

3. Results and discussion

3.1. Materials characterization

3.1.1. Textural and reducibility characteristics

The textural characteristics of the supports and of the corresponding Rh catalysts are summarized in Table 1. It is apparent that differences between the un-metallized and the Rh-containing samples are marginal. Table 1 includes Rh particle sizes of the fresh catalysts as determined by H_2-chemisorption and HRTEM. The good agreement between the results obtained by these independent methods is apparent and the HRTEM results are analyzed further below.

Fig. 1 shows hydrogen consumptions as a function of temperature (H_2-TPR) obtained with calcined γ-Al_2O_3, ACZ and CZ supports and also for the corresponding Rh-loaded catalysts. As expected, no uptake was observed with γ-Al_2O_3 in accordance to its non-reducible character, whereas two broad, overlapped peaks with maxima at ca. 450–500 °C and 650–700 °C were observed for ACZ and CZ. The two-peak feature is characteristic of CeO_2-containing samples. In accord with the literature, the low temperature peak is attributed to $Ce^{4+}\rightarrow Ce^{3+}$ superficial reduction taking place at CZ surfaces, whilst the high temperature feature is attributed to the corresponding reduction of bulk CeO_2 [62]. The relative intensities and profiles of the peaks are characteristic of CeO_2-containing materials with comparatively low surface area [62], as here—see Table 1. The Oxygen Storage Capacities (OSC) of the supports assessed by H_2-TPR (Fig. 1) were 0, 101 and 557 μmol O_2 g^{-1} for γ-Al_2O_3, ACZ and CZ respectively. Dispersion of ~1 wt% Rh on the supports resulted in a significant enhancement of the reducibility of ACZ and CZ as evidenced by the substantial shift of the TPR peaks to lower temperature (ca. 150–450 °C), indicating dramatic promotion of hydrogen spillover, which in the absence of metal is limited by H_2 dissociation. The additional peak at ~ 90 °C is attributed to reduction of Rh_2O_3 to metallic Rh^0. Interaction between cerium and rhodium oxides has been reported to improve the reducibility of both components due to H_2 spillover from rhodium particles inducing concurrent reduction of both CeO_2 and Rh_2O_3 [62,63]. With the non-reducible support (γ-Al_2O_3) the Rh_2O_3 reduction peak appeared at a significantly higher temperature (~150 °C rather than 90 °C, Fig. 1), indicating a reduced extent of hydrogen spillover phenomena in this case. Moreover, as we shall see, in the cases of ACZ and CZ the occurrence of O^{2-} spillover between the support and rhodium particles was confirmed by XPS.

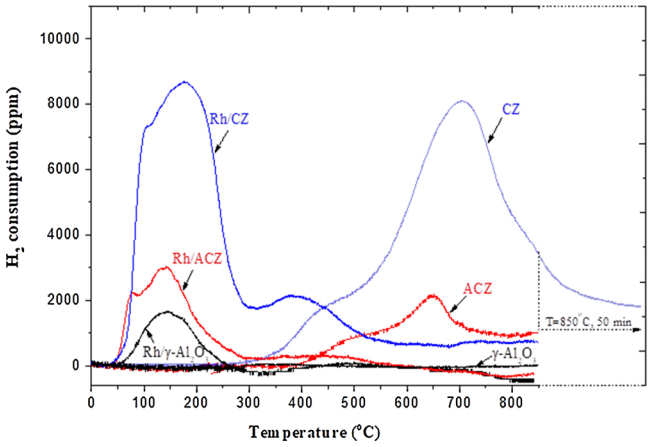

Fig. 1. H_2-TPR profiles of the γ-Al_2O_3, ACZ and CZ supports and the corresponding supported Rh catalysts.

3.1.2. Structural and morphological characteristics

Representative PXRD patterns obtained for fresh Rh/γ-Al_2O_3, Rh/ACZ and Rh/CZ catalysts are shown in Fig. 2. Reflections characteristic of γ-Al_2O_3 at 2θ = 32.6°, 37.2°, 39.5°, 46.0°, 60.9° and 66.9° can be seen in the diffractogram for fresh Rh/γ-Al_2O_3 (Fig. 2, pattern (a)), whilst Fig. 2 pattern (c) shows the characteristic reflections of a CZ solid solution. The ACZ diffractogram illustrated in Fig. 2 pattern (b) contains reflections corresponding to γ-Al_2O_3 and CZ present as distinct phases, consistent with a mutual partial coating of the two substances at the nanometer scale. Earlier studies that made use of ACZ composites synthesized by methods similar to that used here [61,64,65] showed that the presence of Al_2O_3 nanoparticles restricted particle growth of CZ in ACZ and prevented sintering of the dispersed noble metal at elevated temperatures [64]. Diffraction peaks corresponding to Rh-containing phases were undetectable due to the low metal loading and small size of the Rh nanoparticles, as indeed demonstrated by H_2 chemisorption (Table 1) and HRTEM (see below).

Fig. 3 shows representative HRTEM images and the corresponding particle size distributions of the three fresh catalysts. All samples exhibited small, randomly distributed spherical particles with average sizes of 1.3 ± 0.4, 1.5 ± 0.5 and 5.1 ± 1.7 nm for Rh/γ-Al_2O_3, Rh/ACZ and Rh/CZ respectively (Table 1). Formation of smaller Rh

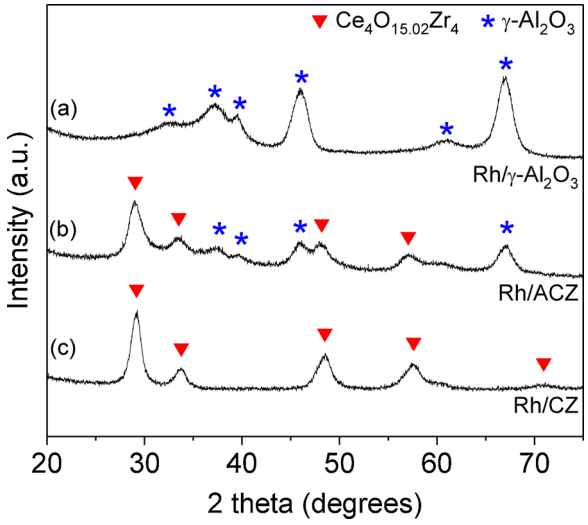

Fig. 2. XRD patterns of fresh (a) Rh/γ-Al_2O_3, (b) Rh/ACZ and (c) Rh/CZ catalysts.

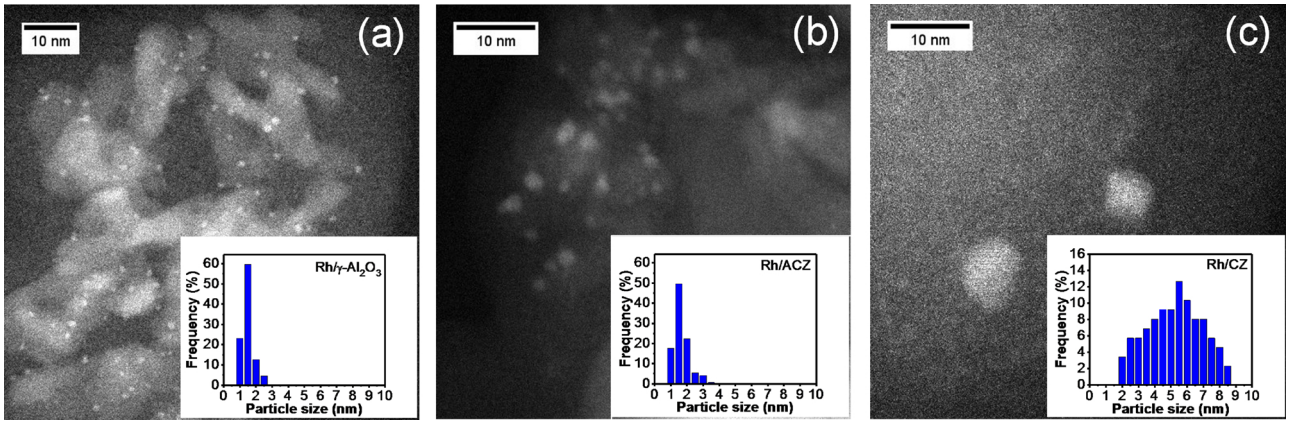

Fig. 3. HRTEM images of fresh Rh/γ-Al_2O_3 (a), Rh/ACZ (b) and Rh/CZ (c) catalysts and the corresponding particle size distribution histograms.

particles on the γ-Al_2O_3-containing supports can be mainly attributed to the larger surface areas of these materials.

3.2. Evaluation of catalytic performance and stability

In order to evaluate catalytic performance and time-on-stream stability, measurements were performed under both integral (high conversion) and differential (low conversion) reaction conditions at a total pressure of 1 bar.

3.2.1. DRM performance under integral conditions

The time-on-stream stability of the three catalysts over a period of 12 h was examined at 750 °C, $CH_4/CO_2 = 1$ (corresponding to typical biogas composition) and a weight-basis gas hourly space velocity (WGHSV = F_t/w_{cat}) equal to 120,000 N mL g^{-1} h^{-1}. Although 12 h may appear to be a relatively short time for stability tests, the literature shows that most of the deterioration of DRM catalysts occurs during the first 1–15 hours (i.e., carbon deposition, particle agglomeration) [20,66]. Moreover, our catalysts were operated for at least 4 days before acquisition of the kinetic data (light-off curves, TOFs, oxidative sintering), during which time periodic activity tests at 750 °C showed very stable performance.

Stability results obtained are illustrated in Fig. 4, which shows the variation with time of CH_4 and CO_2 conversions (X_{CH_4} and X_{CO_2}), H_2 and CO yields (Y_{H_2} and Y_{CO}) and H_2/CO molar ratio.

It is evident that all three catalysts exhibited good stability and performance with respect to all the above reaction parameters; methane conversion was stable over 12 h at ~90% for Rh/γ-Al_2O_3 (Fig. 4a) and ~65-70% for Rh/ACZ (Fig. 4b) and Rh/CZ (Fig. 4c). The lower methane conversion obtained with the latter two catalysts is compatible with their lower Rh content (0.8 wt% vs 1.0 wt% for Rh/γ-Al_2O_3) and also their lower Rh-dispersion values (Table 1). A more detailed and rigorous comparison of catalytic performance in terms of intrinsic activity (i.e. turnover frequencies) is given below. Compared to conventional Ni-based catalysts, [20–26] the good stability of our Rh catalysts can be principally attributed to their much lower propensity for carbon deposition. This view is strongly supported by findings to be discussed below and is in accordance with earlier studies [3,9–11,39–47,67]. It is to be expected that under the strongly reducing environment of DRM, much of the rhodium would be present as Rh^0, as indeed directly demonstrated by the post-reaction XPS results described below.

In order to examine possible effects of the Rh oxidation state on catalytic performance and the necessity or otherwise of H_2 pre-reducing Rh-based catalysts before exposure to reforming reactions (a commonly applied procedure for Ni-based reforming catalysts), consecutive tests were carried out in which the used catalysts were immediately subjected to in situ oxidation (20% O_2/He flow, 2 h, 750 °C) followed by switching back to reaction gas. Rapid and complete restoration of conversion and yield to levels equal to those of the corresponding pre-reduced fresh catalysts was observed (Fig. 4). This indicates that the active sites, presumably Rh^0, are readily regenerated after exposure to reaction conditions. In addition, all catalysts retained their stability after exposure to high temperature oxidative sintering. The lack of necessity for H_2 preconditioning and the good stability under reducing-oxidizing cycles are of significant importance with respect to the use of Rh in cost-efficient catalytic systems for DRM implementation.

Conversion, yield and H_2/CO molar ratio performances as a function of temperature in the range 400–750 °C are summarized in Fig. 5. Although these are broadly similar for the three cases, there are significant differences. Specifically, the H_2/CO molar ratios, < 1.0 in all cases, decrease in the order Rh/γ-Al_2O_3 > Rh/ACZ > Rh/CZ. This reflects the increasing discrepancy between CO_2 and CH_4 conversions, the former varying in the opposite order to the H_2/CO molar ratios. The systematic increase of the relative CO_2 conversion on going from low OSC supports to higher OSC supports ($OSC_{Al_2O_3} < OSC_{ACZ} < OSC_{CZ}$), with a concomitant increase in CO formation relative to H_2, indicates that support-induced modifications of the Rh surface chemistry are responsible. This issue is discussed below in connection with the intrinsic TOF data.

3.2.2. Intrinsic activity

Intrinsic activity results for the catalysts are shown as Arrhenius plots in Figures S2, S3 and S4 (*supplementary material*). Data were acquired under conditions of low methane and carbon dioxide conversions (~5–15%) in order to reflect intrinsic activity, unaffected by mass and/or thermal transport constraints.

Given the large variation in oxygen ion lability between the three supports [56] possible effects of metal-support interactions are of interest. Fig. 6 shows the temperature dependence of turnover frequencies of CH_4 (Fig. 6a) and CO_2 (Fig. 6b) given as moles consumed per mol of active site per second (active sites correspond to surface rhodium atoms calculated by the use of H_2-uptake values obtained from the chemisorption experiments, Table 1). It is apparent that rhodium supported on CZ and ACZ exhibited a better intrinsic activity than Rh/γ-Al_2O_3, with Rh/CZ being the best overall. This may be ascribed to the reduced apparent activation energies (E_a) for CO_2 and CH_4 consumption exhibited by the two catalysts with ceria-containing supports, the effect being more pronounced for CO_2 consumption (Fig. 6b: E_a = 98, 76 and 82 kJ mol^{-1} for Rh/γ-Al_2O_3, Rh/ACZ and Rh/CZ, respectively) compared to CH_4 consumption (Fig. 6a: E_a = 95, 79 and 93 kJ mol^{-1} for Rh/γ-Al_2O_3, Rh/ACZ and Rh/CZ, respectively): this is consistent with a bi-functional reaction mechanism that operated when the support contained labile oxygen. Specifically, surface oxygen vacancies could initiate CO_2 activation by adsorption and scission to CO + O. The

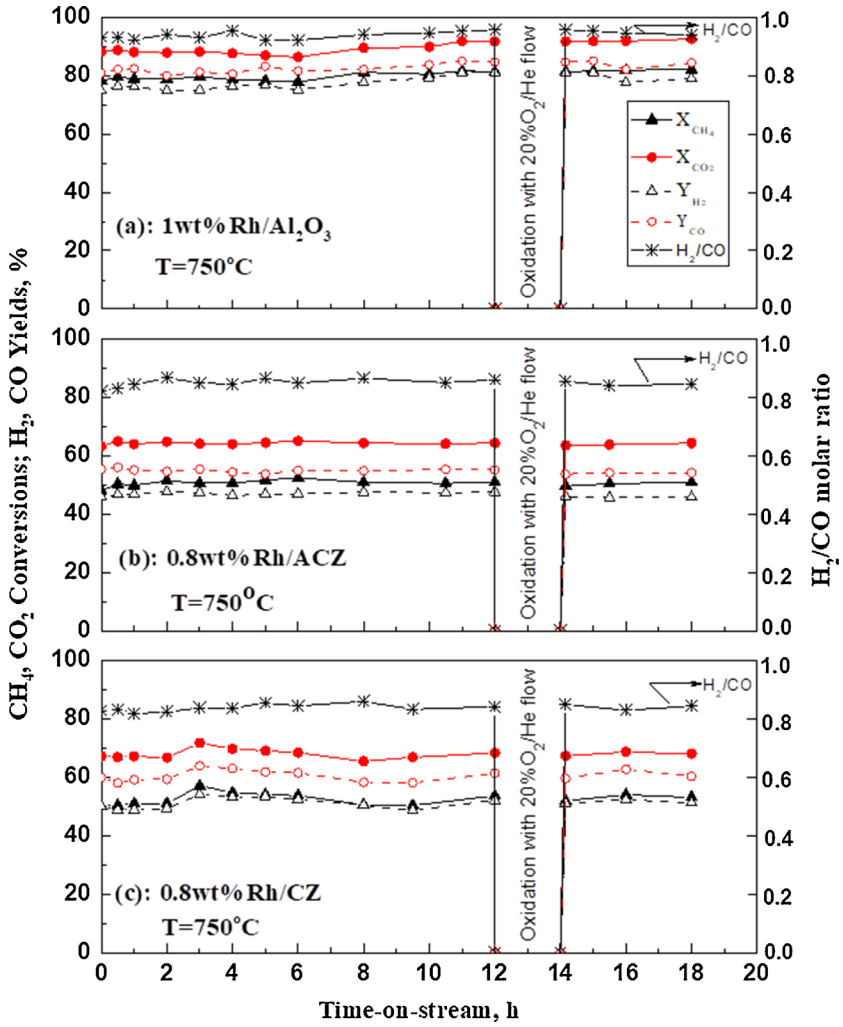

Fig. 4. (CH_4, CO_2)-conversion, (H_2, CO)-yield and H_2/CO molar ratio yields for fresh Rh/γ-Al_2O_3 (a), Rh/ACZ (b) and Rh/CZ (c) catalysts as a function of time on stream at T = 750 °C and equimolar feed ([CH_4] = 50%, [CO_2] = 50%). Experimental conditions: $F_{t,in}$ = 100 N mL min^{-1}; catalyst mass w_{cat} = 50 mg. Note rapid and complete restoration of DRM activity following a 2 h in situ oxidation with 20% O_2/He flow (100 N mL min^{-1}) at 750 °C.

resulting regenerated labile oxygen ions could then promote oxidation of carbon on the support and enhance oxygen ion spillover onto Rh, altering its electronic properties and surface chemistry by metal-support interactions [56] before ultimate reaction as *sacrificial* promoter [57] with CH_4-derived adsorbed carbonaceous species on Rh sites. This interpretation is consistent with the observation of CO-enriched syngas produced by CZ-containing samples (Fig. 6c) and, as described below, with the reduced carbon deposition (TPO and XPS) exhibited by these catalysts. Promotion of the *reverse* water gas shift reaction due the enhanced basicity of ceria-containing supports [3] would also act to increase the CO content of the reformate, as proposed for Ni-based DRM catalysts [20]. From a practical point of view, it is noteworthy that the present results suggest that CeO_2-containing supports could be of value for low temperature DRM, which is a challenging and attractive application [4,5,68–70].

3.3. Characterization of used samples after DRM reaction

3.3.1. Carbon deposition - TPO measurements

The extent of carbon deposition was strongly dependent on the nature of the support, as shown by results of temperature programmed oxidation experiments illustrated in Fig. 7. Here, the amount of CO_2 formed during a linear temperature ramp (10 °C/min) under a stream of 6.1% O_2 in He was monitored after exposure of the fresh catalysts to DRM conditions ([CH_4] = 50%, [CO_2] = 50%, T = 750 °C, F_t = 100 N mL min^{-1}) for 3 h. CO production was negligible in all cases and Table 2 summarizes the results, expressed as μmol C / g catalyst. The extent of carbon deposition was relatively small in all three cases, in accordance with earlier work, confirming the excellent resistance of Rh catalysts to coking under DRM [3,39,44].

The total amount of carbon deposited followed the order Rh/γ-Al_2O_3 > Rh/ACZ > Rh/CZ (Fig. 7 and Table 2), in good accord with the XPS results presented below. Thus increased OSC of the support decreased its propensity to accumulate carbon, in agreement with Djinovic et al. [45]. This effect has been ascribed to the presence of oxygen vacancies (Ce^{4+}/Ce^{3+} redox couple) which activate methane on the Rh surface by metal-support interactions, resulting in a bifunctional reaction mechanism, as noted above.

Apart from its influence on the amount of coke deposition, the identity of the support also affected the nature of the carbon species formed. High oxygen mobility is thought to enhance carbon gasification, thus inhibiting carbide formation and subsequent nucleation and growth of carbon filaments [71].

The TPO profile of Rh/CZ shows a principal peak at ~ 295 °C and two smaller peaks at 110 and 520 °C (Fig. 7). The 110 °C peak can be attributed to reactive superficial carbide species [72–75] while the 295 °C and 520 °C peaks can be ascribed to two different types of amorphous carbonaceous deposits [75]. The intensity of the low-temperature TPO peak was much higher for the Al_2O_3-containing catalysts (Rh/γ-Al_2O_3 and Rh/ACZ) compared to Rh/CZ. This points to a reduced

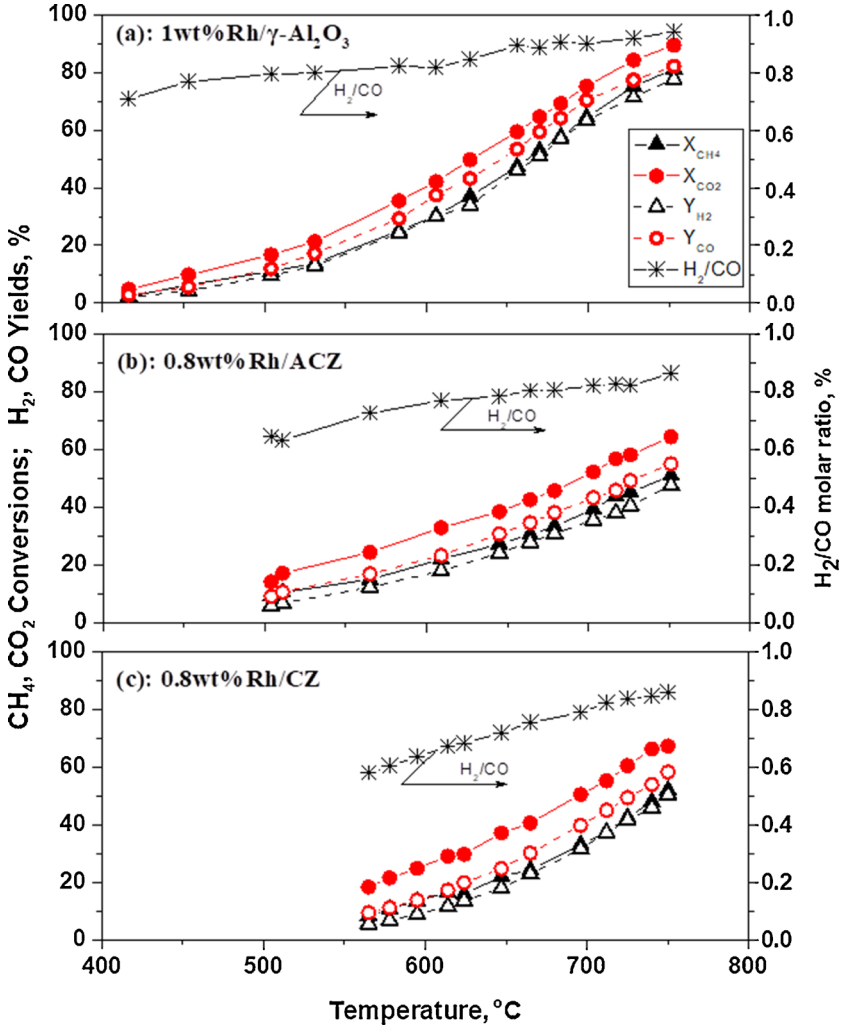

Fig. 5. (CH_4, CO_2)-conversion, (H_2, CO)-yield and H_2/CO molar ratio for fresh Rh/γ-Al_2O_3 (a), Rh/ACZ (b) and Rh/CZ (c) as a function of temperature. Experimental conditions: equimolar feed ([CH_4] = 50%, [CO_2] = 50%); $F_{t,in}$ = 100 N mL min^{-1}; catalyst mass w_{cat} = 50 mg.

activity of these two catalysts for the oxidation of carbidic carbon, previously proposed as a reactive intermediate responsible for the high DRM activity of Rh and Ru [75]. These TPO results are in general agreement with XPS measurements presented below, which clearly show that ceria incorporation suppresses carbide formation–down to zero in the case of the CZ support. The catalysts with ceria-containing supports exhibit smaller high temperature peaks (Fig. 7) compared to Rh/γ-Al_2O_3, in agreement with results of previous studies [51] where they were assigned to pyrolytic carbon resulting from thermal cracking of methane: high oxygen mobility acts to reduce its amount.

3.3.2. XPS results obtained after running under DRM conditions followed by in situ sample transfer without exposure to laboratory air

Fig. 8 shows representative XP spectra of the Rh 3d (Fig. 8a) and C 1 s (Fig. 8b) region of all three catalysts before and after treatment under DRM conditions in the high pressure cell. These spectra provide qualitative and quantitative analysis of the catalyst surfaces, a summary of which is shown in Tables 3 and 4.

The results presented in Fig. 8 and Table 3 show striking differences between the fresh calcined catalysts in regard to the oxidation states of Rh: Rh/ACZ and Rh/γ-Al_2O_3 contained *only* Rh^{3+} whereas Rh/CZ contained both Rh^{3+} and Rh^{1+}. This is a clear evidence of strong metal-support interaction between Rh particles and supports with high oxygen ion lability such as CZ; the absence of Rh^{1+} in the fresh calcined Rh/ACZ is most probably due to the relatively low CZ-content (~20 wt %) in the ACZ, thus limiting interaction between Rh particles and CZ regions. As previously shown by other methods, supports with high oxygen ion lability can substantially destabilize Rh oxide which can then be readily reduced to the metallic state, in contrast to the situation on γ-Al_2O_3 (~ zero oxygen ion lability), where rhodium oxide is stable [76]. O^{2-} spillover characteristic of *active* supports such as those containing ceria results in an electric double layer [$O^{\delta-}$,δ^+] on the surface of Rh particles, previously invoked to explain strong metal-support interactions by analogy with the electric double layer created electrochemically [77], during so-called Electrochemical Promotion or NEMCA effect (Non-Faradaic Electrochemical Modification of Catalytic Activity) [58,78].

After exposure to DRM conditions, the three catalysts again displayed substantial differences with respect to Rh oxidation states and also in regard to the amounts of Rh carbide present (Fig. 8a). Rh/CZ *contained* 100% Rh^0 *and no detectable carbide*. (The feature at 303.2 eV labeled in Fig. 8a with a * is the Ce (M_3VV) Auger line [79]). Rh/ACZ contained 72% Rh^0, the remainder being largely Rh^{3+} along with a small amount of Rh carbide. Rh/γ-Al_2O_3 contained the least Rh^0 of all (ca. 55%), significant Rh^{3+}, and twice as much Rh carbide as Rh/ACZ. Clearly, incorporation of CZ in the support acts to (i) maintain Rh in the metallic state and (ii) minimize Rh carbide accumulation under DRM reaction conditions. It also acts to minimize the amount of deposited carbon in all forms, as shown in Fig. 8b and Table 4 which gives the absolute total atomic concentration of carbon in the three

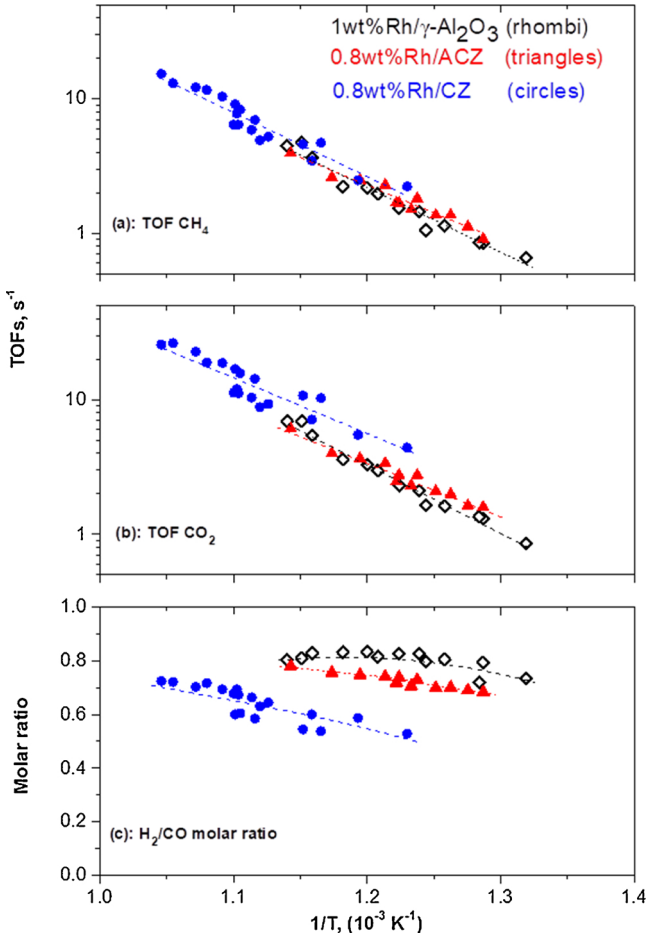

Fig. 6. Temperature dependence of TOFs of CH_4 (a) and CO_2 (b) consumption, and H_2/CO molar ratio (c) obtained for fresh Rh/Al_2O_3, Rh/ACZ and Rh/CZ catalysts. Experimental conditions: equimolar composition ([CH_4] = 50%, [CO_2] = 50%); catalyst mass w_{cat} = 50 mg.

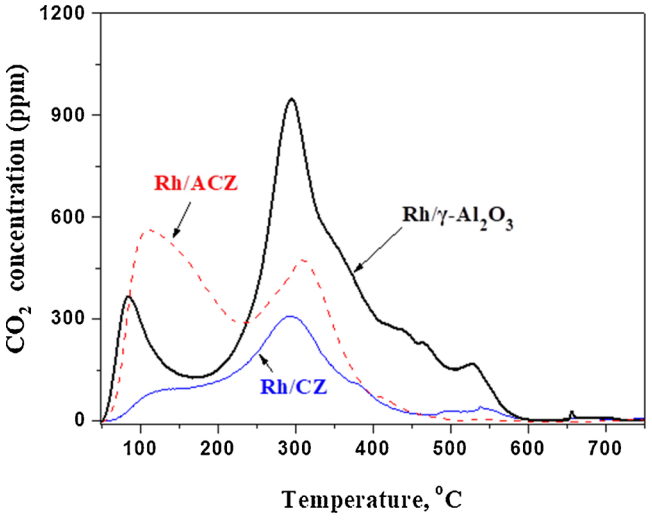

Fig. 7. Temperature programmed oxidation after exposure of fresh catalysts to DRM for 3 h. Temperature ramp 10 °C min^{-1} from room temperature to 750 °C.

catalysts—note that these results are in good accord with the TPO data presented above: *this increases confidence in the direct relevance of the XPS data to the results that were acquired by conventional reactor methods.*

Table 2
Total amount of carbon deposited and mean deposition rate after 3 h of DRM operation.

Catalyst	Total amount of carbon deposited (μmol C / g_{cat})	Mean deposition rate (μmol C / h g_{cat})
Rh/γ-Al_2O_3	221	73.7
Rh/ACZ	168	56.0
Rh/CZ	78	26.0

3.3.3. HRTEM after DRM

HRTEM images and the corresponding rhodium particle size distributions of the post DRM catalysts are shown in Fig. 9. These clearly show that there were no significant changes as compared to the fresh samples (Fig. 3). The average rhodium particle sizes on the Rh/γ-Al_2O_3, Rh/ACZ and Rh/CZ catalysts were 1.7 ± 0.4, 2.9 ± 1.2 and 5.4 ± 1.7 nm respectively. Comparing these values with those of the fresh catalysts (Table 1) reveals a slight broadening of the particle size distributions, most evident in the case of Rh/ACZ. However, the data clearly demonstrate that the Rh particles were very stable under reaction conditions.

3.4. Mechanistic implications

It is clear that the most active sites were metallic Rh^0: correlation of post reaction XPS with the kinetic data shows that TOF increased with the amount of Rh^0 present in the catalyst (Fig. 6 and Fig. 8a, Table 3). Surface oxygen vacancies in the CZ-containing supports enhanced the activation of CO_2 by dissociative adsorption, thus increasing DRM activity by means of a bi-functional mechanism. This is in line with the higher CO selectivity and the lower apparent activation energies observed, in particular for CO_2 consumption (Figs. 4–6). The extent and nature of deposited carbon revealed by TPO and XPS were in accord with the activity characteristics of the catalysts and an overall mechanism that is consistent with the results may be derived from them. It is in line with the superior turnover activity of Rh on the CZ-containing supports and implies the operation of a bi-functional reaction pathway.

It is well known that CH_4 and CO_2 activation during DRM follow different routes [20,27,47]: CH_4 is mainly activated on metal sites (M*) that lead to H_2(g) evolution and carbonaceous species, CH_x (reaction 12), and eventually carbide that can transform to filamentous, amorphous, graphite, or whiskers of carbon [20,27], through the following consecutive steps (12) [27]:

$$CH_4(g) \overset{+M^*}{\rightarrow} CH_4 - M^* \overset{+M^*}{\rightarrow} CH_3 - M^* + H - M^* \overset{+M^*}{\rightarrow} CH_2 - M^* + 2\,H - M^* \overset{+M^*}{\rightarrow} CH - M^* + 3\,H - M^* \overset{+M^*}{\rightarrow} C - M^* + 4\,H - M^* \overset{-4M^*}{\rightarrow} C - M^* + 2H2(g) \quad (12)$$

CO_2 is activated by dissociative adsorption to CO + O on both metal and support sites, the latter especially favorable in the case of CeO_2-containing supports incorporating a significant concentration of oxygen vacancies, $V_{\ddot{O}}$, via the following steps (13) [27]:

$$CO_2\,(g) + V_{\ddot{O}} \rightarrow O_i'' + CO\,(g) \quad (13)$$

thus supplying oxygen atoms to the support forming interstitial (labile) O^{2-} ions, O_i''; these eventually occupy oxygen vacancies ($V_{\ddot{O}}$ and O_i'': Kröger-Vink notation for point defects and interstitial oxygen ions, respectively [56,78]).

Reaction (13) is also responsible for the CO-enriched reformate (Figs. 2–6) produced by Rh/ACZ and Rh/CZ compared to Rh/γ-Al_2O_3.

The concentration of the oxygen ion vacancies is determined by the equilibrium [56,78]:

$$O_O \leftrightarrow V_{\ddot{O}} + O_i'' \quad (14)$$

between lattice oxygen, O_O, and interstitial oxygen ions, O_i'' (i.e. O^{2-}

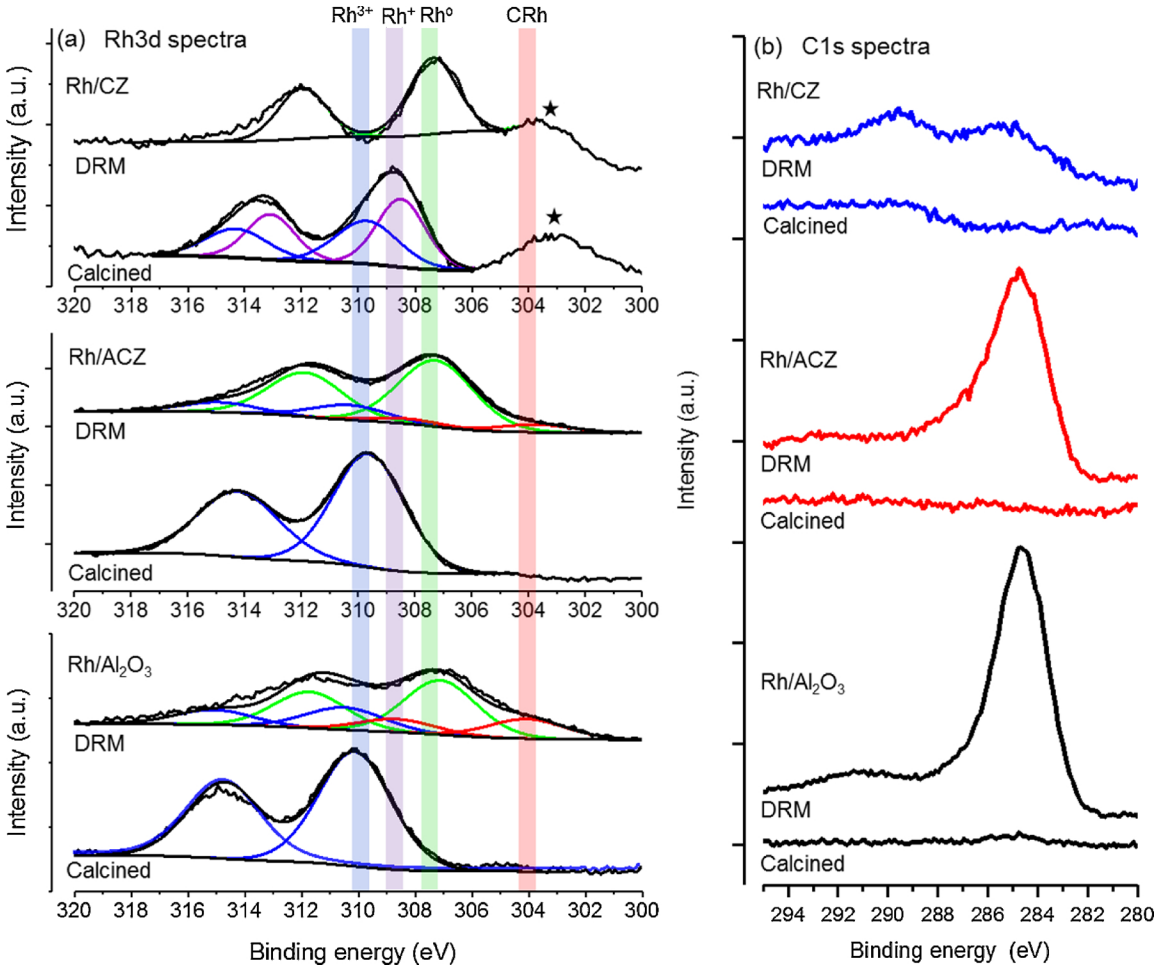

Fig. 8. XPS spectra corresponding to (a) Rh 3d and (b) C1 s regions obtained before and after in situ DRM over the indicated catalyst samples. The feature labeled with a * in the Rh 3d spectra corresponds to a Ce Auger transition.

Table 3
Oxidation states of rhodium prior to and after in situ DRM obtained from deconvolution of Rh 3d spectra. B.E. of the components used in each fitting is indicated in brackets.

Sample	% Rh Carbide (B.E. / eV)	% Rh^0 (B.E. /eV)	%Rh^{1+} (B.E. /eV)	% Rh^{3+} (B.E. /eV)
Rh/γ-Al_2O_3, fresh[a]	–	–	–	100% (310.1)
Rh/γ-Al_2O_3, after DRM[b]	21% (304.1)	55% (307.1)	–	24% (310.5)
Rh/ACZ, fresh[a]	–	–	–	100% (309.6)
Rh/ACZ, after DRM[b]	10% (304.1)	72% (307.1)	–	18% (310.5)
Rh/CZ, fresh[a]	–	–	55%(308.5)	45% (309.7)
Rh/CZ, after DRM[b]	0% (304.1)	100% (307.2)	–	0% (310.5)

[a] Fresh samples that had been oxidized in air at 750 °C for 2 h before acquisition of XP spectra.
[b] Spent samples, i.e. samples operated under DRM conditions (CH_4:CO_2 = 1:1) at 700 °C for 3 h and moved directly into the XPS chamber without exposure to laboratory air.

Table 4
Atomic surface composition of Rh and C prior and after in situ DRM by indicated catalysts, obtained from XPS spectra plotted in Fig. 8.

Catalyst	XPS atomic concentration	
	Rh	C 1 s
Rh/γ-Al_2O_3, fresh-calcined	0.5	0.6
Rh/γ-Al_2O_3, after DRM	0.5	18.1
Rh/ACZ, fresh-calcined	0.7	0.1
Rh/ACZ, after DRM	0.7	7.4
Rh/CZ, fresh-calcined	0.5	0.2
Rh/CZ, after DRM	0.4	5.1

which corresponds to the redox cycle Ce^{3+}/Ce^{4+} characteristic of CeO_2-containing supports [36–38]).

Oxygen ions back-spillover can then occur onto the surfaces of Rh particles through the following step (15) [80]:

$$O_i^{||} + Rh^* \rightarrow [O^{\delta-}, \delta^+]Rh^* + V_{\ddot{O}} \quad (15)$$

where Rh* denotes a rhodium active site, not exclusively Rh^0 but also RhOx [81].

According to the double-layer account of promotion and metal-support interactions [56–60,78,80], oxygen back-spillover provides an effective double layer [$O^{\delta-}$, δ^+] (with $\delta \approx 2$ [80]) on the Rh particles

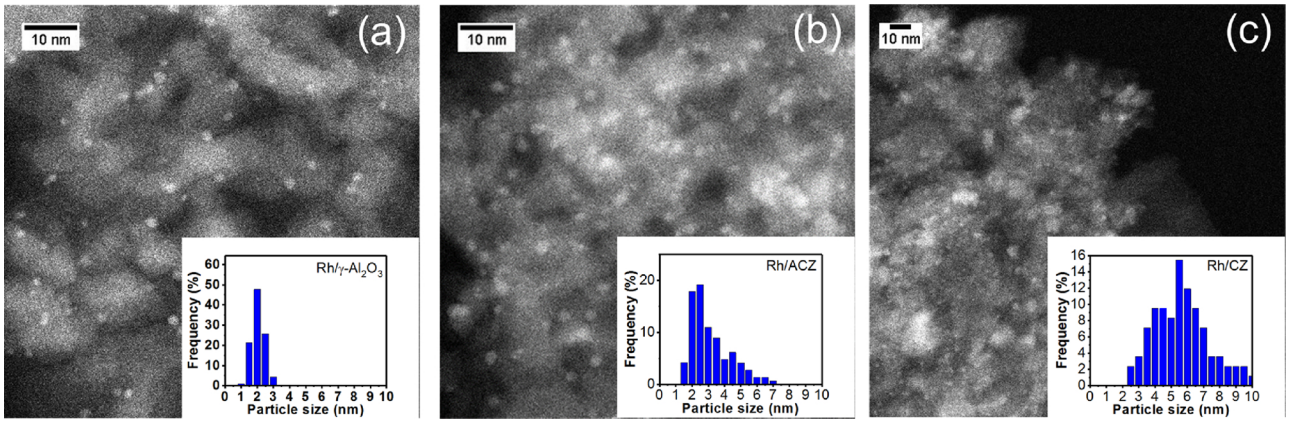

Fig. 9. HRTEM images of the post DRM Rh/γ-Al_2O_3 (a), Rh/ACZ (b) and Rh/CZ (c) catalysts and the corresponding particle size distribution histograms.

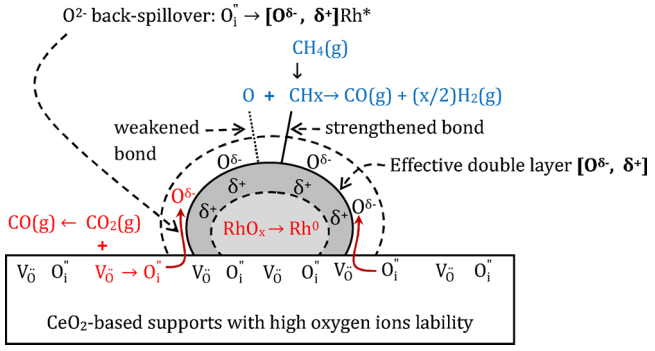

Fig. 10. Model of the bifunctional support-mediated promotion of DRM by supports with high oxygen ion lability.

(Fig. 10), altering their work function and chemisorptive properties and hence their intrinsic activity towards catalytic reactions [56–60,78,80].

In the present case the $O^{\delta-}$ layer increases the Rh work function, weakening the chemisorptive bond of electron acceptor (electrophilic) adsorbates and strengthening that of electron donors (electrophobes).

Accordingly, the Rh-O bond is weakened (atomic O is an electron acceptor), destabilizing the RhOx state and promoting its transformation to Rh^0 (Fig. 8a, Table 3) while the chemisorption bonds of CH_4, and carbonaceous species derived from it, are strengthened because of their electrophilic character [78], thus promoting CH_4 activation via reaction (12). The $[O^{\delta-}, \delta^+]Rh^*$ double layer displaces O(a) to a more weakly bound and therefore more reactive state, enhancing the intrinsic activity of Rh particles supported on high oxygen lability supports, as indeed observed. The decreased apparent activation energies found for Rh/ACZ and Rh/CZ catalysts are in agreement with this view.

According to the *sacrificial promoter* concept [57,80], $O^{\delta-}$ species on the Rh surface, are themselves reactive and are rapidly consumed by the oxidizable reactants present (CH_4 and species derived from it). They are nevertheless effective because they are continuously replenished by labile O^{2-} species provided by the support. At very high temperatures, where the lifetime of $O^{\delta-}$ species is significantly shortened [40], their promotional effect is correspondingly diminished. The Arrhenius diagrams in Fig. 6 are consistent with this: at high temperatures (> 750 °C) the intrinsic activity of Rh/γ-Al_2O_3 approached that of Rh/ACZ and Rh/CZ. This promotional effect is therefore favored at low temperatures, once again indicating that CZ is a promising support for low temperature DRM.

4. Conclusions

Results of a detailed investigation of the effect of different oxide supports, with or without high oxygen ion lability, on important catalytic parameters (activity, selectivity, stability, resistance to carbon deposition, oxidative aging) relevant to DRM enabled construction of an overall reaction mechanism.

State of the art XPS measurements, never used previously in DRM studies, were especially revealing. These results show unambiguously and for the first time what the oxidation states of Rh actually are and how they can vary during DRM. Also, how the degree of oxygen lability of the supports affects this key trait.

The principal active metal site is unambiguously identified as Rh^0: Rh_2O_3 is destabilized by supports with high oxygen lability due to O^{2-} backspillover that weakens the Rh-O bond. This effect also accounts for reduced carbon deposition on ACZ and especially, CZ-supported Rh. Interestingly, on CZ, Rh^0 persists even under oxidizing atmospheres.

A new bi-functional mechanism for DRM promotion based on the "effective double layer model" of metal-support interactions, fits well with the observations. Methane activation occurs on Rh^0 sites. In the case of CZ-containing supports, dissociative adsorption of CO_2 is promoted at oxygen vacancies in the support.

Kinetic data indicate that Rh shows promise as a low temperature DRM catalyst, a challenging and attractive potential application.

In regard to methodology, it is shown that energy-consuming hydrogen preconditioning is not necessary for the activation of Rh-based DRM catalysts, unlike Ni-based catalysts.

Acknowledgements

This work was co-funded by the European Union and Greek national funds through the Operational Program "Competitiveness, Entrepreneurship and Innovation", under the call "RESEARCH-CREATE-INNOVATE" (project code: T1EΔK-00782). G.K. acknowledges funding from the Royal Society and EPSRC (EP/M005186/2).

Appendix A. Supplementary data

Supplementary material related to this article can be found, in the online version, at doi:https://doi.org/10.1016/j.apcatb.2018.10.048.

References

[1] J.-M. Lavoie, Review on dry reforming of methane, a potentially more environmentally-friendly approach to the increasing natural gas exploitation, Front. Chem. 2 (2014) 81, https://doi.org/10.3389/fchem.2014.00081.
[2] X.E. Verykios, Catalytic dry reforming of natural gas for the production of chemicals and hydrogen, Int. J. Hydrog. Energy 28 (2003) 1045–1063, https://doi.org/10.1016/S0360-3199(02)00215-X.
[3] D. Pakhare, J. Spivey, A review of dry (CO_2) reforming of methane over noble metal catalysts, Chem. Soc. Rev. 43 (2014) 7813–7837, https://doi.org/10.1039/c3cs60395d.
[4] N.A.K. Aramouni, J.G. Touma, B.A. Tarboush, J. Zeaiter, M.N. Ahmad, Catalyst design for dry reforming of methane: analysis review, Renew. Sust. Energy Rev. 82

(2018) 2570–2585, https://doi.org/10.1016/j.rser.2017.09.076.
[5] B. Abdullah, N.A.A. Ghani, D.-V.N. Vo, Recent advances in dry reforming of methane over Ni-based catalysts, J. Clean. Prod. 162 (2017) 170–185. https://doi.org/10.1016/j.jclepro.2017.05.176.
[6] Y. Wang, L. Yao, S. Wang, D. Mao, C. Hu, Low-temperature catalytic CO_2 dry reforming of methane on Ni-based catalysts: a review, Fuel Process. Technol. 169 (2018) 199–206, https://doi.org/10.1016/j.fuproc.2017.10.007.
[7] I.V. Yentekakis, G. Goula, Biogas management: advanced utilization for production of renewable energy and added-value chemicals, Front. Environ. Sci. 5 (2017) 7, https://doi.org/10.3389/fenvs.2017.00007.
[8] P. Panagiotopoulou, C. Papadopoulou, H. Matralis, X.E. Verykios, Production of renewable hydrogen by reformation of biofuels, Wiley Interdiscip. Rev. Energy Environ. 3 (2014) 231–253, https://doi.org/10.1002/wene.93.
[9] W.K. Jóźwiak, M. Nowosielska, J. Rynkowski, Reforming of methane with carbon dioxide over supported bimetallic catalysts containing Ni and noble metal: I. Characterization and activity of SiO_2 supported Ni–Rh catalysts, Appl. Catal. A Gen. 280 (2005) 233–244, https://doi.org/10.1016/j.apcata.2004.11.003.
[10] H.Y. Wang, E. Ruckenstein, Carbon dioxide reforming of methane to synthesis gas over supported rhodium catalysts: the effect of support, Appl. Catal. A Gen. 204 (2000) 143–152, https://doi.org/10.1016/S0926-860X(00)00547-0.
[11] U.L. Portugal, A.C.S.F. Santos, S. Damyanova, C.M.P. Marques, J.M.C. Bueno, CO_2 reforming of CH_4 over Rh-containing catalysts, Mol. Catal. A: Chem. 184 (2002) 311–322, https://doi.org/10.1016/S1381-1169(02)00018-3.
[12] E. Le Saché, L. Pastor-Pérez, D. Watson, A. Sepúlveda-Escribano, T.R. Reina, Ni stabilised on inorganic complex structures: superior catalysts for chemical CO_2 recycling via dry reforming of methane, Appl. Catal. B: Environ. 236 (2018) 458–465, https://doi.org/10.1016/j.apcatb.2018.05.051.
[13] S.M. Kim, P.M. Abdala, T. Margossian, D. Hosseini, L. Foppa, A. Armutlulu, W. van Beek, A. Comas-Vives, C. Copéret, C. Müller, Cooperativity and dynamics increase the performance of NiFe dry reforming catalysts, J. Am. Chem. Soc. 139 (2017) 1937–1949, https://doi.org/10.1021/jacs.6b11487.
[14] F. Zhang, Z. Liu, S. Zhang, N. Akter, R.M. Palomino, D. Vovchok, I. Orozco, D. Salazar, J.A. Rodriguez, J. Llorca, J. Lee, D. Kim, W. Xu, A.I. Frenkel, Y. Li, T. Kim, S.D. Senanayake, In situ elucidation of the active state of Co–Ceox catalysts in the dry reforming of methane: the important role of the reducible oxide support and interactions with cobalt, ACS Catal. 8 (2018) 3550–3560, https://doi.org/10.1021/acscatal.7b03640.
[15] I.V. Yentekakis, Open- and closed-circuit study of an intermediate temperature SOFC directly fueled with simulated biogas mixtures, J. Power Sources 160 (2006) 422–425, https://doi.org/10.1016/j.jpowsour.2005.12.069.
[16] I.V. Yentekakis, T. Papadam, G. Goula, Electricity production from wastewater treatment via a novel biogas-SOFC aided process, Solid State Ion. 179 (2008) 1521–1525, https://doi.org/10.1016/j.ssi.2007.12.049.
[17] Y. Shiratori, T. Ijichi, T. Oshima, K. Sasaki, Internal reforming SOFC running on biogas, Int. J. Hydrog. Energy 35 (2010) 7905–79012, https://doi.org/10.1016/j.ijhydene.2010.05.064.
[18] L. Barelli, A. Ottaviano, Solid oxide fuel cell technology coupled with methane dry reforming: a viable option for high efficiency plant with reduced CO_2 emissions, Energy 71 (2014) 118–129, https://doi.org/10.1016/j.energy.2014.04.070.
[19] M.K. Nikoo, N.A.S. Amin, Thermodynamic analysis of carbon dioxide reforming of methane in view of solid carbon formation, Fuel Process. Technol. 92 (2011) 678–691, https://doi.org/10.1016/j.fuproc.2010.11.027.
[20] M.A. Goula, N.D. Charisiou, G. Siakavelas, L. Tzounis, I. Tsiaoussis, P. Panagiotopoulou, G. Goula, I.V. Yentekakis, Syngas production via the biogas dry reforming reaction over Ni supported on zirconia modified with CeO_2 or La_2O_3 catalysts, Int. J. Hydrog. Energy 42 (2017) 13724–13740, https://doi.org/10.1016/j.ijhydene.2016.11.196.
[21] Z. Zhang, X.E. Verykios, Carbon dioxide reforming of methane to synthesis gas over supported Ni catalysts, Catal. Today 21 (1994) 589–595, https://doi.org/10.1016/0920-5861(94)80183-5.
[22] Z. Zhang, X.E. Verykios, S.M. MacDonald, S. Affrossman, Comparative study of carbon dioxide reforming of methane to synthesis gas over Ni/La_2O_3 and conventional nickel-based catalysts, J. Phys. Chem. 100 (1996) 744–754, https://doi.org/10.1021/jp951809e.
[23] S. Barama, C. Dupeyrat-Batiot, M. Capron, E. Bordes-Richard, O. Bakhti-Mohammedi, Catalytic properties of Rh, Ni, Pd and Ce supported on Al-pillared montmorillonites in dry reforming of methane, Catal. Today 141 (2009) 385–392, https://doi.org/10.1016/j.cattod.2008.06.025.
[24] X. Li, D. Li, H. Tian, L. Zeng, Z.-J. Zhao, J. Gong, Dry reforming of methane over Ni/La_2O_3 nanorod catalysts with stabilized Ni nanoparticles, Appl. Catal. B: Environ. 202 (2017) 683–694, https://doi.org/10.1016/j.apcatb.2016.09.071.
[25] A. Serrano-Lotina, L. Daza, Long-term stability test of Ni-based catalyst in carbon dioxide reforming of methane, Appl. Catal. A Gen. 474 (2014) 107–113, https://doi.org/10.1016/j.apcata.2013.08.027.
[26] T. Stroud, T.J. Smith, E. Le Saché, J.L. Santos, M.A. Centeno, H. Arellano-Garcia, J.A. Odriozola, T.R. Reina, Chemical CO_2 recycling via dry and bi reforming of methane using Ni-Sn/Al_2O_3 and Ni-Sn/CeO_2-Al_2O_3 catalysts, Appl. Catal. B: Environ. 224 (2018) 125–135, https://doi.org/10.1016/j.apcatb.2017.10.047.
[27] M.M. Makri, M.A. Vasiliades, K.C. Petallidou, A.M. Efstathiou, Effect of support composition on the origin and reactivity of carbon formed during dry reforming of methane over 5 wt% Ni/$Ce_{1-x}M_xO_{2-\delta}$ (M = Zr^{4+}, Pr^{3+}) catalysts, Catal. Today 259 (2015) 150–164, https://doi.org/10.1016/j.cattod.2015.06.010.
[28] W.D. Zhang, B.S. Liu, Y.L. Tian, CO_2 reforming of methane over Ni/Sm_2O_3–CaO catalyst prepared by a sol–gel technique, Catal. Commun. 8 (2007) 661–667, https://doi.org/10.1016/j.catcom.2006.08.020.
[29] M.H. Amin, K. Mantri, J. Newnham, J. Tardio, S.K. Bhargava, Highly stable ytterbium promoted Ni/γ-Al_2O_3 catalysts for carbon dioxide reforming of methane, Appl. Catal. B: Environ. 119 (2012) 217–226, https://doi.org/10.1016/j.apcatb.2012.02.039.
[30] W. Chen, G. Zhao, Q. Xue, L. Chen, Y. Lu, High carbon-resistance Ni/$CeAlO_3$-Al_2O_3 catalyst for CH_4/CO_2 reforming, Appl. Catal. B: Environ. 136-137 (2013) 260–268, https://doi.org/10.1016/j.apcatb.2013.01.044.
[31] P. Kumar, Y. Sun, R.O. Idem, Nickel-Based Ceria, Zirconia, and Ceria–Zirconia catalytic systems for low-temperature carbon dioxide reforming of methane, Energy Fuels 21 (2007) 3113–3123, https://doi.org/10.1021/ef7002409.
[32] X. Xiang, H. Zhao, J. Yang, J. Zhao, L. Yan, H. Song, L. Chou, Nickel based mesoporous silica-ceria-zirconia composite for carbon dioxide reforming of methane, Appl. Catal. A Gen. 520 (2016) 140–150, https://doi.org/10.1016/j.apcata.2016.04.020.
[33] A. Wolfbeisser, O. Sophiphum, J. Bernardi, J. Wittayakun, K. Fottinger, G. Rupprechter, Methane dry reforming over ceria-zirconia supported Ni catalysts, Catal. Today 277 (2016) 234–245, https://doi.org/10.1016/j.cattod.2016.04.025.
[34] E.C. Faria, R.C.R. Neto, R.C. Colman, F.B. Noronha, Hydrogen production through CO_2 reforming of methane over Ni/$CeZrO_2$/Al_2O_3 catalysts, Catal. Today 228 (2014) 138–144, https://doi.org/10.1016/j.cattod.2013.10.058.
[35] J.A. Rodriguez, D.C. Grinter, Z. Liu, R.M. Palomino, S.D. Senanayake, Ceria-based model catalysts: fundamental studies on the importance of the metal–ceria interface in CO oxidation, the water–gas shift, CO_2 hydrogenation, and methane and alcohol reforming, Chem. Soc. Rev. 46 (2017) 1824–1841, https://doi.org/10.1039/C6CS00863A.
[36] J. Kaspar, P. Fornasiero, M. Graziani, Use of CeO_2-based oxides in the three-way catalysis, Catal. Today 50 (1999) 285–298, https://doi.org/10.1016/S0920-5861(98)00510-0.
[37] A.S. Ivanova, Physicochemical and catalytic properties of systems based on CeO_2, Kinet. Catal. 50 (2009) 797–815, https://doi.org/10.1134/S0023158409060020.
[38] I.V. Yentekakis, M. Konsolakis, P. Granger, V.I. Parvulescu, W. Prellier (Eds.), Three-Way Catalysis" in Perovskites and Related Mixed Oxides: Concepts and Applications, Wiley-VCH Verlag GmbH & Co. KGaA, Weinheim, Germany, 2016.
[39] A.T. Ashcroft, A.K. Cheetham, M.L.H. Green, P.D.F. Vernon, Partial oxidation of methane to synthesis gas using carbon dioxide, Nature 352 (1991) 225–226, https://doi.org/10.1038/352225a0.
[40] I.V. Yentekakis, G. Goula, P. Panagiotopoulou, A. Katsoni, E. Diamadopoulos, D. Mantzavinos, A. Delimitis, Dry reforming of methane: catalytic performance and stability of ir catalysts supported on γ-Al_2O_3, $Zr_{0.92}Y_{0.08}O_{2-\delta}$ (YSZ) or $Ce_{0.9}Gd_{0.1}O_{2-\delta}$ (GDC) supports, Top. Catal. 59 (2015) 1228–1241, https://doi.org/10.1007/s11244-015-0490-x.
[41] R. Wang, H. Xu, X. Liu, Q. Ge, W. Li, Role of redox couples of Rh^0/Rh^{8+} and Ce^{4+}/Ce^{3+} in CH_4/CO_2 reforming over Rh–CeO_2/Al_2O_3 catalyst, Appl. Catal. A Gen. 305 (2006) 204–210, https://doi.org/10.1016/j.apcata.2006.03.021.
[42] A.M. Efstathiou, A. Kladi, V.A. Tsipouriari, X.E. Verykios, Reforming of methane with carbon dioxide to synthesis gas over supported rhodium catalysts: II. A steady-state tracing analysis: mechanistic aspects of the carbon and oxygen reaction pathways to form CO, J. Catal. 158 (1996) 64–75, https://doi.org/10.1006/jcat.1996.0006.
[43] Z.L. Zhang, V.A. Tsipouriari, A.M. Efstathiou, X.E. Verykios, Methane with carbon dioxide to synthesis gas over supported rhodium catalysts: I. Effects of support and metal crystallite size on reaction activity and deactivation characteristics, J. Catal. 158 (1996) 51–63, https://doi.org/10.1006/jcat.1996.0005.
[44] Z. Hou, P. Chen, H. Fang, X. Zheng, T. Yashima, Production of synthesis gas via methane reforming with CO_2 on noble metals and small amount of noble-(Rh-) promoted Ni catalysts, Int. J. Hydrog. Energy 31 (2006) 555–561, https://doi.org/10.1016/j.ijhydene.2005.06.010.
[45] P. Djinovic, J. Batista, A. Pintar, Efficient catalytic abatement of greenhouse gases: methane reforming with CO_2 using a novel and thermally stable Rh–CeO_2 catalyst, Int. J. Hydrog. Energy 37 (2012) 2699–2707, https://doi.org/10.1016/j.ijhydene.2011.10.107.
[46] K. Großmann, T. Dellermann, M. Dillig, J. Karl, Coking behavior of nickel and a rhodium based catalyst used in steam reforming for power-to-gas applications, Int. J. Hydrog. Energy 42 (2017) 11150–11158, https://doi.org/10.1016/j.ijhydene.2017.02.073.
[47] S. Cimino, L. Lisi, G. Mancino, Effect of phosphorous addition to Rh-supported catalysts for the dry reforming of methane, Int. J. Hydrog. Energy 42 (2017) 23587–23598, https://doi.org/10.1016/j.ijhydene.2017.04.264.
[48] P. Ferreira-Aparicio, M. Fernandez-Garcia, A. Guerrero-Ruiz, I. Rodriguez-Ramos, Evaluation of the role of the metal–Support interfacial centers in the dry reforming of methane on alumina-supported rhodium catalysts, J. Catal. 190 (2000) 296–308, https://doi.org/10.1006/jcat.1999.2752.
[49] S. Yokota, K. Okumura, M. Niwa, Support effect of metal oxide on Rh catalysts in the CH_4-CO_2 reforming reaction, Catal. Lett. 84 (2002) 131–134, https://doi.org/10.1023/A:1021097206196.
[50] A. Nematollahi, M. Rezaei, M. Khajenoori, Combined dry reforming and partial oxidation of methane to synthesis gas on noble metal catalysts, Int. J. Hydrog. Energy 36 (2011) 2969–2978, https://doi.org/10.1016/j.ijhydene.2010.12.007.
[51] A. Moral, I. Reyero, G. Alfaro, F. Bimbela, L.M. Gandia, Syngas production by means of biogas catalytic partial oxidation and dry reforming using Rh-based catalysts, Catal. Today 299 (2018) 280–288, https://doi.org/10.1016/j.cattod.2017.03.049.
[52] A. Song, W. Pan, Tri-reforming of methane: a novel concept for catalytic production of industrially useful synthesis gas with desired H_2/CO ratios, Catal. Today 98 (2004) 463–484, https://doi.org/10.1016/j.cattod.2004.09.054.
[53] T.J. Siang, T.L.M. Pham, N.V. Cuong, P.T.T. Phuong, N.H.H. Phuc, Q.D. Truong, D.-V.N. Vo, Compined steam and CO2 reforming of methane for syngas production over carbon-resistant boron-promoted Ni/SBA-15 catalysts, Microporous

Mesoporous Mater. 262 (2018) 122–132, https://doi.org/10.1016/j.micromeso.2017.11.028.
[54] S. Cimino, G. Landi, L. Lisi, G. Russo, Development of a dual functional structured catalyst for partial oxidation of methane to syngas, Catal. Today 105 (2005) 718–723, https://doi.org/10.1016/j.cattod.2005.06.058.
[55] Z. Yuan, C. Ni, C. Zhang, D. Gao, S. Wang, Y. Xie, A. Okada, Rh/MgO/$Ce_{0.5}Zr_{0.5}O_2$ supported catalyst for autothermal reforming of methane: the effects of ceria–zirconia doping, Catal. Today 146 (2009) 124–131, https://doi.org/10.1016/j.cattod.2009.02.032.
[56] P. Vernoux, L. Lizarraga, M.N. Tsampas, F.M. Sapountzi, A. De Lucas-Consuegra, J.-L. Valverde, S. Souentie, C.G. Vayenas, D. Tsiplakides, S. Balomenou, E.A. Baranova, Ionically conducting ceramics as active catalyst supports, Chem. Rev. 113 (2013) 8192–8260, https://doi.org/10.1021/cr4000336.
[57] C.G. Vayenas, Promotion, electrochemical promotion and metal–support interactions: their common features, Catal. Lett. 143 (2013) 1085–1097, https://doi.org/10.1007/s10562-013-1128-x.
[58] C.G. Vayenas, S. Ladas, S. Bebelis, I.V. Yentekakis, S. Neophytides, Y. Jiang, Ch. Karavasilis, C. Pliangos, Electrochemical promotion in catalysis: non-faradaic electrochemical modification of catalytic activity, Electrochim. Acta 39 (1994) 1849–1855, https://doi.org/10.1016/0013-4686(94)85174-3.
[59] I.V. Yentekakis, G. Goula, P. Panagiotopoulou, S. Kampouri, M.J. Taylor, G. Kyriakou, R.M. Lambert, Stabilization of catalyst particles against sintering on oxide supports with high oxygen ion lability exemplified by Ir-catalyzed decomposition of N_2O, Appl. Catal. B: Environ. 192 (2016) 357–364, https://doi.org/10.1016/j.apcatb.2016.04.011.
[60] I.V. Yentekakis, G. Goula, S. Kampouri, I. Betsi-Argyropoulou, P. Panagiotopoulou, M.J. Taylor, G. Kyriakou, R.M. Lambert, Ir-catalysed nitrous oxide (n_2o) decomposition: effect of Ir particle size and metal–support interactions, Catal. Lett. 148 (2018) 341–347, https://doi.org/10.1007/s10562-017-2233-z.
[61] A. Papavasiliou, A. Tsetsekou, V. Matsuka, M. Konsolakis, I.V. Yentekakis, An investigation of the role of Zr and La dopants into $Ce_{1-x-y}Zr_xLa_yO_8$ enriched γ-Al_2O_3 TWC washcoats, Appl. Catal. A Gen. 382 (2010) 73–84, https://doi.org/10.1016/j.apcata.2010.04.025.
[62] P. Fornasiero, R. Di Monte, G. Ranga Rao, J. Kaspar, S. Meriani, A. Trovarelli, M. Graziani, Rh-loaded CeO_2-ZrO_2 solid-solutions as highly efficient oxygen exchangers: dependence of the reduction behavior and the oxygen storage capacity on the structural-properties, J. Catal. 151 (1995) 168–177, https://doi.org/10.1006/jcat.1995.1019.
[63] M. Ozawa, M. Takahashi-Morita, K. Kobayashi, M. Haneda, Core-shell type ceria zirconia support for platinum and rhodium three way catalysts, Catal. Today 281 (2017) 482–489, https://doi.org/10.1016/j.cattod.2016.06.029.
[64] A. Morikawa, T. Suzuki, T. Kanazawa, K. Kikuta, A. Suda, H. Shinjo, A new concept in high performance ceria–zirconia oxygen storage capacity material with Al_2O_3 as a diffusion barrier, Appl. Catal. B: Environ. 78 (2008) 210–221, https://doi.org/10.1016/j.apcatb.2007.09.013.
[65] F.A. Silva, D.S. Martinez, J.A.C. Ruiz, L.V. Mattos, C.H. Hori, F.B. Noronha, The effect of the use of cerium-doped alumina on the performance of Pt/CeO_2/Al_2O_3 and Pt/$CeZrO_2$/Al_2O_3 catalysts on the partial oxidation of methane, Appl. Catal. A Gen. 335 (2008) 145–152, https://doi.org/10.1016/j.apcata.2007.11.003.
[66] N.D. Charisiou, G. Siakavelas, L. Tzounis, V. Sebastian, A. Monzon, M.A. Baker, S.J. Hinder, K. Polychronopoulou, I.V. Yentekakis, M.A. Goula, Inter. J. Hydr. Energy 43 (2018) 18955–18976, https://doi.org/10.1016/j.ijhydene.2018.08.074.
[67] Y.T. Shah, T.H. Gardner, Dry reforming of hydrocarbon feedstocks, Catal. Rev. Sci. Eng. 56 (2014) 476–536, https://doi.org/10.1080/01614940.2014.946848.
[68] R.K. Singha, A. Yadav, A. Shukla, M. Kumar, R. Bal, Low temperature dry reforming of methane over Pd-CeO_2 nanocatalyst, Catal. Commun. 92 (2017) 19–22, https://doi.org/10.1016/j.catcom.2016.12.019.
[69] Y. Wang, L. Yao, S. Wang, D. Mao, C. Hu, Low temperature catalytic CO_2 reforming of methane on Ni-based catalysts: a review, Fuel Process. Technol. 169 (2018) 199–206, https://doi.org/10.1016/j.fuproc.2017.10.007.
[70] A. Lofberg, J. Guerrero-Caballero, T. Kane, A. Rubbens, L. Jalowiecki-Duhamel, Ni/CeO_2 based catalysts as oxygen vectors for the chemical looping dry reforming of methane for syngas production, Appl. Catal. B: Environ. 212 (2017) 159–174, https://doi.org/10.1016/j.apcatb.2017.04.048.
[71] R.C. Rabelo-Neto, H.B.E. Sales, C.V.M. Inocêncio, E. Varga, A. Oszko, A. Erdohelyi, F.B. Noronha, L.V. Mattos, CO_2 reforming of methane over supported $LaNiO_3$ perovskite-type oxides, Appl. Catal. B: Environ. 221 (2018) 349–361, https://doi.org/10.1016/j.apcatb.2017.09.022.
[72] C.H. Bartholomew, Carbon Deposition in Steam Reforming and Methanation, Catal. Rev. Sci. Eng. 24 (1982) 67–112, https://doi.org/10.1080/03602458208079650.
[73] C. Mirodatos, H. Praliaud, M. Primet, Deactivation of nickel-based catalysts during CO methanation and disproportionation, J. Catal. 107 (1987) 275–287, https://doi.org/10.1016/0021-9517(87)90294-6.
[74] H.M. Swaan, V.C.H. Kroll, G.A. Martin, C. Mirodatos, Deactivation of supported nickel catalysts during the reforming of methane by carbon dioxide, Catal. Today 21 (1994) 571–578, https://doi.org/10.1016/0920-5861(94)80181-9.
[75] M. Rezaei, S.M. Alavi, S. Sahebdelfar, Z.F. Yan, Syngas production by methane reforming with carbon dioxide on noble metal catalysts, J. Nat. Gas. Chem. 15 (2006) 327–334, https://doi.org/10.1016/S1003-9953(07)60014-0.
[76] A. Pliangos, I.V. Yentekakis, V.G. Papadakis, C.G. Vayenas, X.E. Verykios, Support-induced promotional effects on the activity of automotive exhaust catalysts: 1. The case of oxidation of light hydrocarbons (C_2H_4), Appl. Catal. B: Environ 14 (1997) 161–173, https://doi.org/10.1016/S0926-3373(97)00020-9.
[77] J. Nicole, D. Tsiplakides, C. Pliangos, X.E. Verykios, Ch. Comninellis, C.G. Vayenas, Electrochemical promotion and metal-support interactions, J. Catal. 204 (2001) 23–34, https://doi.org/10.1006/jcat.2001.3360.
[78] C.G. Vayenas, S. Bebelis, I.V. Yentekakis, H.-G. Lintz, Non-faradaic electrochemical modification of catalytic activity: a status report, Catal. Today 11 (1992) 303–438, https://doi.org/10.1016/0920-5861(92)80002-5.
[79] A. Gayen, K.R. Priolkar, P.R. Sarode, V. Jayaram, M.S. Hegde, G.N. Subbanna, S. Emura, $Ce_{1-x}Rh_xO_{2-\delta}$ solid solution formation in combustion-synthesized Rh/CeO_2 catalyst studied by XRD, TEM, XPS, and EXAFS, Chem. Mater. 16 (2004) 2317–2328, https://doi.org/10.1021/cm040126l.
[80] C.G. Vayenas, S. Brosda, C. Pliangos, The double-layer approach to promotion, electrocatalysis, electrochemical promotion, and metal–support interactions, J. Catal. 216 (2003) 487–504, https://doi.org/10.1016/S0021-9517(02)00127-6.
[81] S. Parres-Esclapez, I. Such-Basanez, M.J. Illan-Gomez, C. Salinas-Martinez de Lecea, A. Bueno-Lopez, Study by isotopic gases and in situ spectroscopies (DRIFTS, XPS and Raman) of the N_2O decomposition mechanism on Rh/CeO_2 and Rh/γ-Al_2O_3 catalysts, J. Catal. 276 (2010) 390–401, https://doi.org/10.1016/j.jcat.2010.10.001.